Journal of Energy Chemistry 76 (2023) 165–174

Contents lists available at ScienceDirect

Journal of Energy Chemistry

journal homepage: www.elsevier.com/locate/jechem

http://www.journals.elsevier.com/journal-of-energy-chemistry/

Interconnected and high cycling stability polypyrrole supercapacitors using cellulose nanocrystals and commonly used inorganic salts as dopants

Zuxin Sun, Wim Thielemans *

Sustainable Materials Lab, Department of Chemical Engineering, KU Leuven, Campus Kulak Kortrijk, Etienne Sabbelaan 53, 8500 Kortrijk, Belgium

ARTICLE INFO

Article history:
Received 21 June 2022
Revised 5 September 2022
Accepted 12 September 2022
Available online 17 September 2022

Keywords:
Polypyrrole
Cellulose nanocrystals
Cycling stability
Inorganic salts
Supercapacitor

ABSTRACT

Polypyrrole (PPy) is wildly used as electrode material in supercapacitors due to its high conductivity, low cost, ease of handling, and ease of fabrication. However, limited capacitance and poor cycling stability hinder its practical application. After developing carboxylated cellulose nanocrystals (CNC-COO^-) as immobile dopants for PPy to improve its cycling stability, we investigated the effect of different commonly used salts (KCl, NaCl, KBr, and $NaClO_4$) as dopants during electrode fabrication by electropolymerization. The film's capacitance increased from 160.6 to 183.4 F g^{-1} after adding a combination of KCl and $NaClO_4$ into the electrodeposition electrolyte. More importantly, the porous and interconnected PPy/CNC-COO^--Cl^-(ClO_4^-)_0.5 electrode film exhibited an excellent capacitance of 125.0 F g^{-1} (0.78 F cm^{-2}) at a high current density of 2.0 A g^{-1} (20 mA cm^{-2}, allowing charging in less than 1 min), increasing almost 204% over PPy/CNC-COO^- films. A symmetric PPy/CNC-COO^--Cl^-(ClO_4^-)_0.5 supercapacitor retained its full capacitance after 5000 cycles, and displayed a high energy density of 5.2 Wh kg^{-1} at a power density of 25.4 W kg^{-1} (34.5 μWh cm^{-2} at 1752.3 μW cm^{-2}). These results reveal that the porous structure formed by doping with CNC-COO^- and inorganic salts opens up more active reaction areas to store charges in PPy-based films as the stiff and ribbon-like CNC-COO^- as permanent dopants improve the strength and stability of PPy-based films. Our demonstration provides a simple and practical way to deposit PPy based supercapacitors with high capacitance, fast charging, and excellent cycling stability.

1. Introduction

Polypyrrole (PPy), as one of the most promising pseudocapacitor electrode materials, has attracted a large research interest due to its low cost, high electrical conductivity, environmental friendliness, and wide potential window [1–5]. PPy can be easily polymerized from its water-soluble monomer, which provides opportunities to obtain different structures and properties by adjusting the solutions' composition. By adding different acid dopants (hydrochloride acid, perchloric acid, sulfuric acid, p-toluenesulfonic acid_p-TSA, phosphoric acid, and phytic acid) into the electropolymerization electrolyte, PPy films with different structures and electrochemical performance were obtained after deposition on carbon cloth [6]. Among them, the PPy_HCl/carbon cloth film exhibited the highest specific capacitance of 960 F g^{-1} at 5 mV s^{-1}, the PPy_p-TSA/carbon cloth film showed the best cycling stability (75% capacitance retention after 2000 cycles). By introducing two-dimensional (2D) graphene oxide (GO) into a pyrrole and $LiClO_4$ electrolyte, a three-dimensional (3D) GO/PPy composite electrode was fabricated by one-step electrodeposition [7], achieving an area capacitance of 387.6 mF cm^{-2} (380 F g^{-1}) at 0.2 mA cm^{-2} (0.2 A g^{-1}) and a better rate capability (82%) than for pure PPy electrodes (42.6%). Meanwhile, higher performance PPy composite electrodes can be fabricated by combining PPy with capacitive and/or structural materials, such as graphene oxide, carbon nanotubes, transitional metal compounds, 2D layered clays, and metal–organic frameworks (MOFs) [8–14]. A PPy/$Ti_3C_2T_x$ film showed a specific capacitance of 420.2 F g^{-1} at 1 A g^{-1}, which is almost four times as high as the value for a pristine PPy film prepared using the same method, because of the 2D layered structure of the clay ($Ti_3C_2T_x$) template [9].

Although PPy possesses plenty of merits and has excellent performance as pseudocapacitive material, in practical applications, the cycling stability of PPy electrodes or supercapacitors (SCs) still poses serious challenges due to its working mechanism [2,3,15–

* Corresponding author.
E-mail address: Wim.Thielemans@kuleuven.be (W. Thielemans).

https://doi.org/10.1016/j.jechem.2022.09.024

18]. Tremendous efforts to improve the cycling stability of PPy-based materials have been taken [15,19–22]. One of these methods is templating PPy with flexible substrates that can limit structural damage by adapting to large volumetric changes during charge/discharge cycles. The other method is to dope PPy with immobile anions, which could minimize the counterion drain effect. For example, by using functionalized partial-exfoliated graphite as a scaffold and immobile β-naphthalene sulfonate anions as dopants, fabricated PPy films achieved 97.5% capacitance retention after 10,000 charge/discharge cycles [23].

Our previous work also showed that immobile carboxylated cellulose nanocrystals (CNC-COO^-) contribute to building PPy SCs with high cycling stability, e.g., at a scan rate of 50 mV s^{-1}, 86% of the original capacitance was retained after 1000 cycles, 70% capacitance was retained after 10,000 cycles, and 47% of its capacity after an excessive 50,000 cycles [24]. By adding KCl into the pyrrole (Py) and CNC-COO^- electrodeposition electrolyte, more homogeneous, porous, and interconnected PPy SCs were fabricated, giving a maximum energy density of 41.15 μWh cm^{-2} (4.46 Wh kg^{-1}) and 111.2% of the initial capacitance after 3000 cycles. It suggests that KCl not only serves as a supporting electrolyte for the electropolymerization of PPy, but that it also contributes to the development of the 3D porous structure when combined with CNC-COO^-. The relatively high cycling stability of PPy films is ascribed to the interconnected porous structure and the rigid and immobile CNC-COO^- [25]. Cellulose nanocrystals (CNCs) are the ribbon-like crystalline sections of cellulose that are obtained from native cellulose by hydrolyzing the non-crystalline sections. Their high strength, lightweight, wide availability, ribbon-like morphology, and modifiable surfaces make them interesting reinforcing materials to form porous hierarchical structures [26–28].

In this work, we investigated the effect of different types of commonly used inorganic salts (potassium chloride-KCl, sodium chloride-NaCl, potassium bromide-KBr, and sodium perchlorate-$NaClO_4$) as supporting electrolyte/dopant in the CNC-COO^- and Py electrodeposition electrolyte on structure formation and electrochemical performance of the PPy films. To optimize the performance of the PPy/CNC-COO^--salt composites films, ratios of different types of salts were adjusted in the electrolyte. The film capacitance increased from 160.6 to 183.4 F g^{-1} after adding a combination of KCl and $NaClO_4$ into the electrodeposition electrolyte. The porous and interconnected PPy/CNC-COO^--Cl^-(ClO_4^-)_0.5 electrode film exhibited an excellent capacitance of 125.0 F g^{-1} (0.78 F cm^{-2}) at a high current density of 2.0 A g^{-1} (20 mA cm^{-2}) where the discharge process was completed in one minute. After assembling into a symmetric PPy/CNC-COO^--Cl^-(ClO_4^-)_0.5 supercapacitor, it could retain its full capacitance after 5000 cycles, and displayed a high energy density of 5.2 Wh kg^{-1} at a power density of 25.4 W kg^{-1} (34.5 μWh cm^{-2} at 1752.3 μW cm^{-2}).

2. Experimental

2.1. Materials

Cotton wool was purchased from Carl Roth GmbH & Co. KG. Sodium hydroxide (extra pure), and acetone (98%) were purchased from Fisher Scientific. Ethanol (absolute), sodium perchlorate (98%), and sodium bromide (99%) were purchased from Sigma Aldrich. Sodium hypochlorite (10%–15%), (2,2,6,6-tetramethylpiperidin-l-yl)oxyl (TEMPO, 98%), hydrochloric acid (37%), methanol (98%), pyrrole (99%), potassium chloride (3 M), and sodium chloride (99.999%) were purchased from VWR international. Potassium bromide (99%) was purchased from Acros Organics. All products were used as received.

2.2. Preparation of PPy/CNC-COO^--salt composite films

CNCs were extracted from cotton wool using a modified Araki method (see supporting information) [29]. Through TEMPO-oxidation, the surface hydroxyl groups of CNCs were converted into the carboxyl group as previously described [25,30]. PPy/CNC-COO^--salt composite films were deposited in a three-electrode system. A 3 mm diameter glassy carbon electrode (GCE), a Ag/AgCl (3 M KCl) electrode, and a Pt sheet electrode served as the working, reference, and counter electrode, respectively. Before use, the GCE was polished with alumina (1.0, 0.3 μm) slurries on a polishing pad and rinsed with deionized water before deposition. The electrodeposition electrolyte for deposition PPy/CNC-COO^--salt films contained 160.7 mM Py, and 27 mM of different types of salts (KCl, NaCl, KBr, and $NaClO_4$) in a 13.4 mM CNC-COO^- suspension (Table 1). Electrolytes for deposition PPy/CNC-COO^--Cl^-(ClO_4^-)_x (where x is the ratio of [$NaClO_4$]/[KCl]) films, the concentration of Py, CNC-COO^-, and the total concentration of salt remained the same, only the salt ratio (x) was adjusted. The chronoamperometry method was applied to deposit PPy/CNC-COO^--salt films, +0.8 V potential corresponding to the Ag/AgCl (3 M KCl), and the deposition was stopped when the total passed charge reached 30 C cm^{-2}. The film's area was measured by SEM. Film's weight was measured by a microbalance (XP6 Micro and Ultra-Microbalances, Mettler Toledo) with an accuracy of 1 μg. Detailed information can be found in Fig. S1.

2.3. Fabrication of aqueous symmetric supercapacitors

Aqueous symmetric SCs were constructed by directly assembling two PPy/CNC-COO^--salt films on GCEs, connected in a tube cell with 1 M KCl as the electrolyte. The gap between electrodes and the tube was sealed with parafilm. The mass (area) of two films on the GCE for the PPy/CNC-COO^--ClO_4^- SC and PPy/CNC-COO^--Cl^-(ClO_4^-)_0.5 SC were 1.44 mg (0.24 cm^2) and 1.39 mg (0.21 cm^2), respectively.

2.4. Materials and electrochemical characterization

For the CNC-COO^- suspension, the concentration was determined by thermogravimetric analysis (TGA, Netzsch F3 Tarsus, Table S1). The degree of carboxylation was measured by conductometric titration using an automatic conductometric titrator (Metrohm, 856 conductivity module), showing that CNC-COO^- contained ca. 0.69 mmol g^{-1} surface carboxylate groups after TEMPO-oxidation (Fig. S2). The hydrodynamic diameter and zeta potential of CNC-COO^- were recorded by dynamic light scattering (DLS, Tables S2 and S3) using a NanoBrook particle size and zeta potential analyzer (Brookhaven). The full dataset of characterization results for the CNC-COO^- suspension is available in the Supporting Information.

Morphology of the deposited films was characterized by scanning electron microscopy (SEM, JSM-IT200LV, JEOL, Japan), carried out at an acceleration voltage of 7 or 10 kV. Films were rinsed with distilled water thoroughly and then were gently scraped off from the GCE, which were mounted on aluminum studs with double-sided adhesive carbon tape. No sputtering was performed before imaging. The composition of deposited films was analyzed by energy-dispersive X-ray spectroscopy (EDS, JSM-IT200LV, JEOL, Japan), whole area analysis models were carried out at an acceleration voltage of 20 kV, Std-PC at 50, a magnification of 2500, and live time of 20 min. Fourier transform infrared spectroscopy (FTIR, Bruker Alpha) was used to determine the bond and structure information. Potassium bromide (KBr) was dried in an oven overnight before use. After grinding with mortar, a blank KBr pellet was prepared as the background by a Specac pellet die. A half wt% sample

Table 1
Composition of the electrodeposition electrolyte for different PPy/CNC-COO^--salt films.

Sample	Concentration			Salt type
	Py (mM)	CNC-COO^- (mM)	Salt (mM)	
PPy/Cl^-(K^+)	160.7	N/A	27	KCl
PPy/CNC-COO^-	160.7	13.4	N/A	–
PPy/CNC-COO^--Cl^-(K^+)	160.7	13.4	27	KCl
PPy/CNC-COO^--Cl^-(Na^+)	160.7	13.4	27	NaCl
PPy/CNC-COO^--Br^-	160.7	13.4	27	KBr
PPy/CNC-COO^--ClO_4^-	160.7	13.4	27	$NaClO_4$
PPy/CNC-COO^--Cl^-(ClO_4^-)_0.33	160.7	13.4	20.25(6.75)	KCl + $NaClO_4$
PPy/CNC-COO^--Cl^-(ClO_4^-)_0.5	160.7	13.4	18(9)	KCl + $NaClO_4$
PPy/CNC-COO^--Cl^-(ClO_4^-)_0.67	160.7	13.4	16.2(10.8)	KCl + $NaClO_4$
PPy/CNC-COO^--Cl^-(ClO_4^-)_1.0	160.7	13.4	13.5(13.5)	KCl + $NaClO_4$

was added into the KBr for preparing samples. Spectra were collected as the sum of 64 scans at a resolution of 4 cm^{-1} over a frequency ranging from 4000 to 400 cm^{-1}.

Electrochemical performance of films and SCs were performed at room temperature employing an Autolab PGSTAT204 (Metrohm, NOVA) instrument. One molar KCl was used as the electrolyte. The electrochemical performance of the films was tested in a three-electrode system with a potential window from −0.4 to 0.6 V vs. Ag/AgCl (3 M KCl). The deposited film on GCE was used as the working electrode, where a Ag/AgCl (3 M KCl), and a Pt sheet electrode served as reference and counter electrode, respectively. For SCs, a symmetric two-electrode set-up was built with a potential window from 0 to 1 V. The cyclic voltammetry (CV) experiments were carried out at varying scan rates between 2 and 200 mV s^{-1} for films and SCs. Galvanostatic charge/discharge (GCD) measurements were tested at current densities ranging from 2 to 50 mA cm^{-2} (0.2–5 A g^{-1}) for films, and from 1 to 20 mA cm^{-2} (0.1–2 A g^{-1}) for SCs. The cycling stability of SCs was measured under a current density of 20 mA cm^{-2} (2 A g^{-1}) after resting in 1 M KCl electrolyte for 5 h. Electrochemical impedance spectroscopy (EIS) measurements were carried out over a frequency range of 100 kHz to 0.01 Hz at a potential of 0 V, using an alternating voltage amplitude of 5 mV. The mass loading (mg cm^{-2}) of films was obtained from the total weight of the freestanding film divided by the area of the film measured by SEM (Fig. S1).

The specific capacitance C of the film in a three-electrode system was calculated from cyclic voltammograms according to Eq. (1) [31,32].

$$C = \frac{\int_0^{\frac{2V_0}{v}} |i| dt}{2V_0 \Pi} \quad (1)$$

The specific capacitance C was calculated from GCD according to Eq. (2) [32].

$$C = \frac{I\Delta t}{V_0 \Pi} \quad (2)$$

The equivalent series resistance R_{ES} (Ω), time constant τ (s), energy density E (Wh Π^{-1}), and power density P (W Π^{-1}) of SCs were calculated from GCD according to Eqs. (3)–(6) [32–34].

$$R_{ES} = \frac{\Delta V_{IRdrop}}{I} \quad (3)$$

$$\tau = R_{ES} \times \frac{I\Delta t}{V_0} \quad (4)$$

$$E = \frac{0.5CV_0^2}{3600} \quad (5)$$

$$P = \frac{V_0^2}{4R_{ES}\Pi} \quad (6)$$

where V_0 is the voltage window, v is the scan rate, Π represents the area or the mass of electrodes, where for the three-electrode system, it is the single electrode's mass or area; and for the two-electrode system, it contains the mass or area of both electrodes; I, ΔV_{IRdrop}, and Δt are the discharge current, the voltage of IR drop, and the discharge time, respectively.

3. Results and discussion

3.1. Electrodeposition behavior, morphology, and electrochemical performance of PPy/CNC-COO^--salt films

Fig. 1 shows the synthesis process of PPy/CNC-COO^--salt films. Different commonly used inorganic salts were added to the Py/CNC-COO^- system, the components in the electrodeposition electrolyte are detailed in Table 1. From the chronoamperometric curves in Fig. 1(b), one can see that the presence or absence of salt in the electrolyte led to different deposition behaviors, as discussed in our previous work [25]. In the absence of salt, the deposition current remained close to zero in the first thousand seconds suggesting that the PPy film grew slowly and did not form a continuous structure accommodating electron transfer at the beginning of the deposition process. With salt present in the electrolyte, PPy polymerized more rapidly, with a high current density achieved within a short timeframe. As a result, PPy-based films showed a different morphology in the presence and the absence of salt during deposition (Fig. 1c and d). For different types of salts in the electrolyte, after a sharp increase in current density due to fast nucleation and growth of PPy at the potential step at the outset, the current density showed different tendencies (rising or remaining unchanged), which reflected the influence of different dopants on the formation of PPy composite films due to their different diffusion speeds and sizes.

Fig. 2 shows the morphology of the different PPy/CNC-COO^--salt films. The PPy/Cl^-(K^+) film displayed a globular-shaped structure (Fig. 2a), consistent with previous studies [35–37]. The PPy/CNC-COO^- film showed a relatively dense structure, and at higher magnification (Fig. 2b), one can see that the PPy/CNC-COO^- film is composed of cauliflower-like PPy with plenty of small holes in between. When KCl was added into the pyrrole and CNC-COO^- deposition electrolyte, a porous and interconnected PPy composite film (PPy/CNC-COO^--Cl^-(K^+)) was obtained (Fig. 2c). A similar morphology was obtained when replacing KCl with NaCl or KBr. Both films maintained the porous and interconnected macrostructure (Fig. 2d and e), while the connecting sections in the film with KBr (PPy/CNC-COO^--Br^-) became wider than the connecting sections in PPy/CNC-COO^--Cl^-(K^+) and PPy/CNC-COO^--Cl^-(Na^+) films. With the widening of the connecting sections in the PPy/CNC-COO^--Br^- film, some holes closed. $NaClO_4$, a commonly used supporting electrolyte in the literature, was also explored in our Py

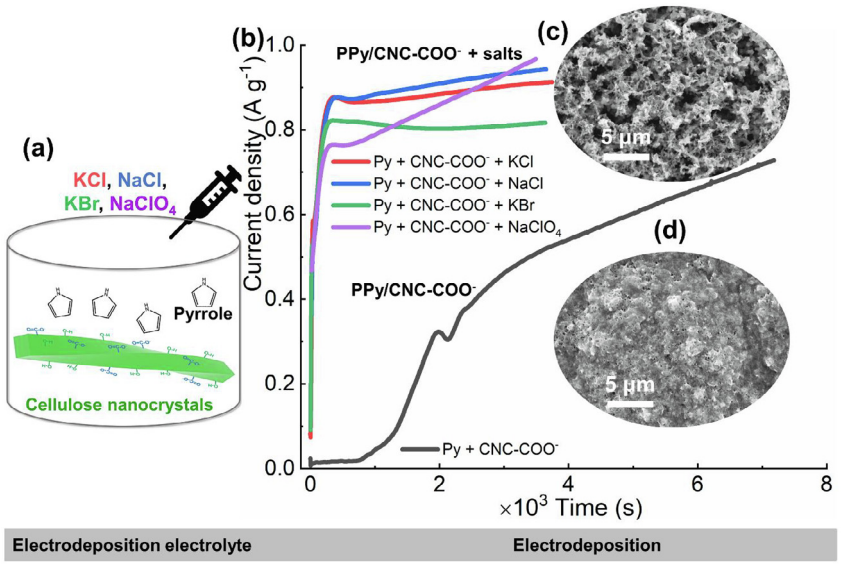

Fig. 1. Schematic illustrating the electrodeposition process of PPy/CNC-COO⁻-salt films. (a) Composition of the electrodeposition electrolyte. (b) Chronoamperometric plots were recorded during deposition with different salts in the electrolyte. SEM images of (c) PPy/CNC-COO⁻ and (d) PPy/CNC-COO⁻-salt films. For each PPy composite film, the deposition stopped until the total passed charge reached 30 C cm^{-2} at the deposited potential of +0.8 V vs. Ag/AgCl (3 M KCl).

and CNC-COO⁻ system [2,20,38,39]. From Fig. 2(f) and its insert image, one can see that the PPy/CNC-COO⁻-ClO_4^- film had a porous and more discrete structure. The formed structure was not as well connected as the PPy/CNC-COO⁻-Cl⁻(K^+), PPy/CNC-COO⁻-Cl⁻(Na^+), and PPy/CNC-COO⁻-Br⁻ films. We can thus conclude that when the electrodeposition electrolyte contained only pyrrole and salt, globular-shaped PPy films were deposited, while deposition in the presence of CNC-COO⁻ and salt, porous PPy films were synthesized, which can be expected to improve the PPy films' electrochemical performance by providing transporting tunnels and reservoirs for electrolyte ions [40].

The elemental composition and bonding information of different PPy/CNC-COO⁻-salt films were determined by EDS and FTIR, respectively. The appearance of nitrogen implies that PPy was embedded in the films (Fig. 3a). Compared to the PPy/Cl⁻(K^+) film, a higher at% of oxygen in other PPy/CNC-COO⁻-salt films indicated that CNC-COO⁻ was incorporated into the films. FTIR spectra (Fig. 3b), show characteristic bands located at 1531–1561 cm^{-1} attributed to the C=C/C–C stretching vibration of the PPy chains. Bands at 1700 and 1299 cm^{-1} represent C=N/C=O and C–N vibrations, matching well with PPy reported in the literature [41,42]. Compared with the PPy/Cl⁻(K^+) film, the intensity of C–O, C–H, and C=O bands for the doped CNC-COO⁻ films are higher, which suggests that CNC-COO⁻ was embedded into the films, in line with changes in the structure.

The electrochemical performance of PPy/CNC-COO⁻ and PPy/CNC-COO⁻-ClO_4^- films in a three-electrode setup showed a pair of broad redox peaks in line with their pseudocapacitive behavior (Fig. 4a). PPy/CNC-COO⁻-Cl⁻(K^+), PPy/CNC-COO⁻-Cl⁻(Na^+), and PPy/CNC-COO⁻-Br⁻ films with more porous and interconnected structures seem to have more capacitive behavior as their CVs approximated a rectangular shape. CVs of PPy/CNC-COO⁻-salt films at other scan rates between 2 and 200 mV s^{-1} are illustrated in Fig. S3. At a current density of 0.5 A g^{-1}, all PPy/CNC-COO⁻-salt films exhibited almost symmetric and linear charge/discharge plots (Fig. 4b), implying the fast charge/discharge process between PPy and electrolyte ions. From the evolution of the specific capacitance with current density (Fig. 4c), one can see that the specific capacitance of the PPy/CNC-COO⁻-ClO_4^- film was significantly higher than for other films at current densities from 0 to 5 A g^{-1}. The highest capacitance reached was 196.1 F g^{-1} at 0.2 A g^{-1} (1.1 F cm^{-2} at 2 mA cm^{-2}, with a mass loading of 5.6 mg cm^{-2}). It increased about 22% compared to the PPy/CNC-COO⁻ film (160.6 F g^{-1} at 0.2 A g^{-1} with a mass loading of 10.2 mg cm^{-2}). The PPy/CNC-COO⁻-Cl⁻(K^+) and PPy/CNC-COO⁻-Cl⁻(Na^+) films had a similar capacitance, especially at high current densities. Comparable results were obtained from the evolution of the specific capacitance with scan rate (Fig. 4d). It suggests that PPy composite films doped with an identical anion had a similar capacitance, while cations have an insignificant effect. The PPy/CNC-COO⁻ and PPy/CNC-COO⁻-Br⁻ films showed a relatively low capacitance.

The EIS behavior of PPy/CNC-COO⁻-salt films is shown in Fig. 4 (e and f). At high frequency (the insert image in Fig. 4e), no obvious semi-circles were observed for any of the films, suggesting a low charge transfer resistance. From the Bode plot of the phase angle against the applied frequency (Fig. 4f), the knee frequency of films is marked at a phase angle of −45° where the film behavior changes from purely resistive to capacitive. The higher the knee frequency, the better the rate capability [43,44]. The knee frequency was 0.02, 0.16, 0.23, and 0.25 Hz, for PPy/CNC-COO⁻-ClO_4^-, PPy/CNC-COO⁻-Cl⁻(K^+), PPy/CNC-COO⁻-Cl⁻(Na^+), and PPy/CNC-COO⁻-Br⁻ films, respectively, which corresponds to 13%, 23%, 24%, and 23% capacitance retention when the scan rate increased from 2 to 200 mV s^{-1}. Hence, the PPy/CNC-COO⁻-ClO_4^- film possessed the worst rate capability. The value of the phase angle indicates the diffusion resistance of electrolyte ions and the electrical resistance of the films [45,46]. The PPy/CNC-COO⁻-Cl⁻(K^+) film had the highest phase angle, i.e., −65° at 0.01 Hz (Fig. 4f), closest to −90° for ideal capacitors. The increase in phase angle implies a smaller diffusion and electrical resistance. The PPy/CNC-COO⁻ film had a large diffusion resistance with a phase angle lower than −40° at the applied frequency. The PPy/CNC-COO⁻-ClO_4^- film also exhibited the same performance as the PPy/CNC-COO⁻ film at frequencies higher than the knee frequency (Fig. 4e). From the electrochemical performance of PPy/CNC-COO⁻-salt films, the PPy/CNC-COO⁻-ClO_4^- film showed the highest specific capacitance, lowest rate capability, and smallest phase angle, while the PPy/CNC-COO⁻-Cl⁻(K^+) film had the largest phase angle (lowest diffusion and electrical resistance). To combine the

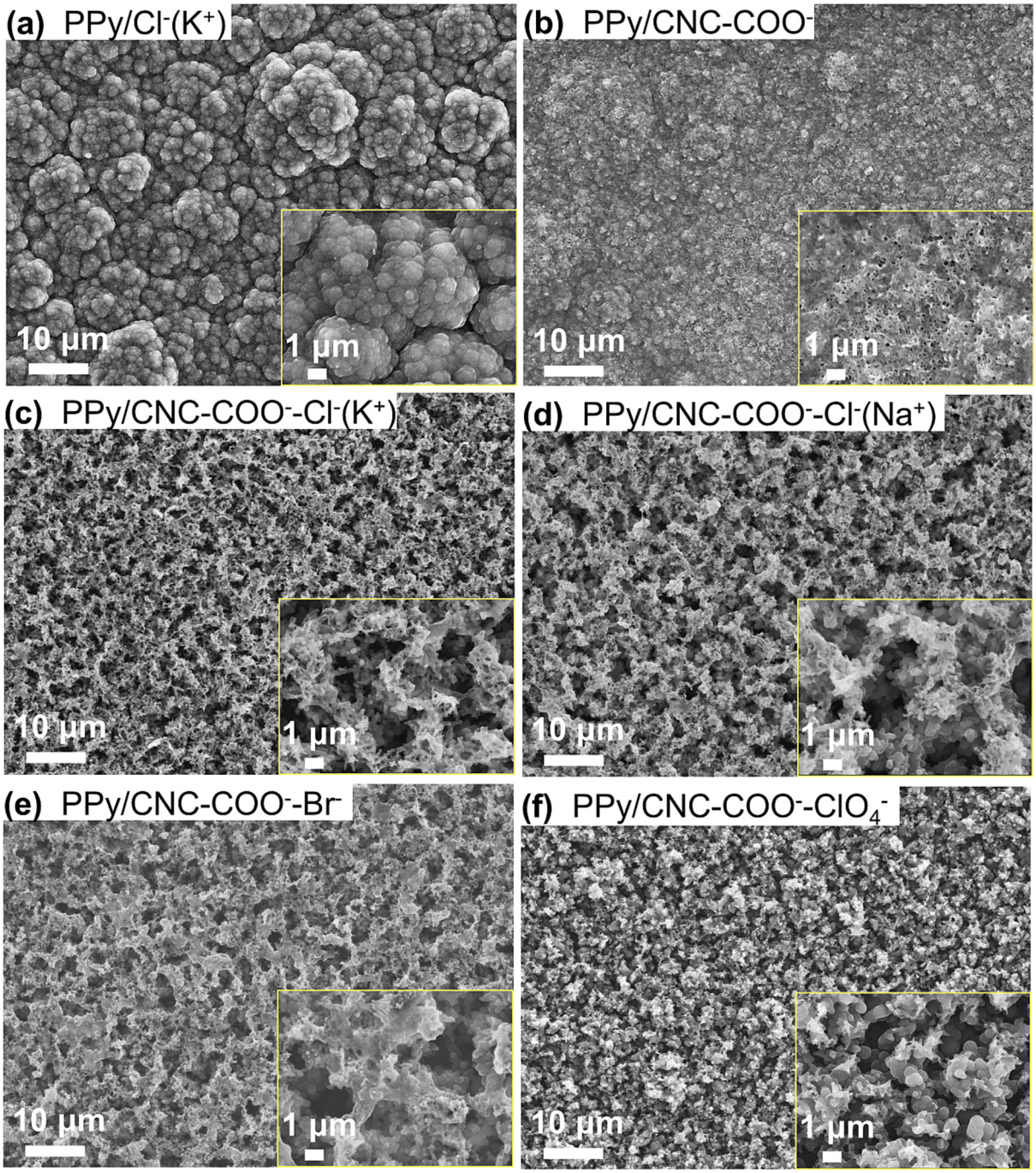

Fig. 2. SEM images of (a) PPy/$Cl^-(K^+)$, (b) PPy/CNC-COO^-, (c) PPy/CNC-COO^--$Cl^-(K^+)$, (d) PPy/CNC-COO^--$Cl^-(Na^+)$, (e) PPy/CNC-COO^--Br^-, and (f) PPy/CNC-COO^--ClO_4^- composite films. The insert is a high magnification image of the corresponding film. Each film was deposited at +0.8 V vs. Ag/AgCl (3 M KCl) reference electrode until the total charge passed was 30 C cm^{-2}.

high capacitance of the ClO_4^--doped films with the high rate capability of the Cl^--doped films, we set out to create films doped with ClO_4^- and Cl^- simultaneously.

3.2. Morphology and electrochemical performance of PPy/CNC-COO^--$Cl^-(ClO_4^-)$ films deposited at different ratios of $NaClO_4$ to KCl

Different ratios of $NaClO_4$ to KCl were added to the Py/CNC-COO^- electropolymerization solution while keeping the total salt concentration constant at 27 mM as before. The detailed composition of the electrodeposition electrolytes is shown in the bottom half of Table 1. The chronoamperometric plots of PPy/CNC-COO^--$Cl^-(ClO_4^-)$ films during deposition are shown in Fig. S4. All films exhibited similar deposition behaviors as for the PPy/CNC-COO^--ClO_4^- film deposition (Fig. 1b). The morphology of the deposited PPy/CNC-COO^--$Cl^-(ClO_4^-)$_0.5 film changed from the discrete PPy/CNC-COO^--ClO_4^- film structure (Fig. 2f) to the more interconnected structure (Fig. 5a and b) seen for PPy/CNC-COO^--$Cl^-(K^+)$ films (Fig. 2c). PPy/CNC-COO^--$Cl^-(ClO_4^-)$ films with other ClO_4^-:Cl^- ratios (Fig. S5) presented a comparable porous and interconnected structure to the PPy/CNC-COO^--$Cl^-(ClO_4^-)$_0.5 films (Fig. 5a and b). From the CV plots of PPy/CNC-COO^--$Cl^-(ClO_4^-)$ films (Fig. 5c), one can see that with increasing $NaClO_4$ in the electrolyte, the height of the broad oxidation and reduction peak increased (as

(a)

Sample \ Element (at%)	C	N	O	Cl	Br
PPy/Cl⁻(K⁺)	64.49	25.06	6.53	3.93	N/A
PPy/CNC-COO⁻	61.49	18.77	17.80	1.88	0.06
PPy/CNC-COO⁻-Cl⁻(K⁺)	58.93	23.88	15.10	1.74	0.34
PPy/CNC-COO⁻-Cl⁻(Na⁺)	62.96	27.97	7.30	1.75	0.02
PPy/CNC-COO⁻-Br⁻	63.55	26.23	7.27	0.13	2.82
PPy/CNC-COO⁻-ClO_4^-	60.15	25.78	12.44	1.58	0.04

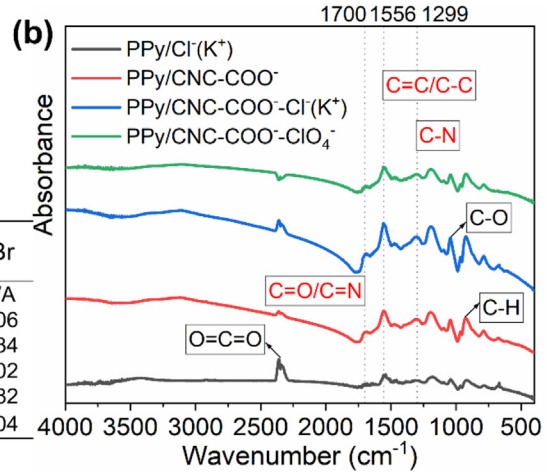

Fig. 3. (a) EDS and (b) FTIR results of PPy/CNC-COO⁻-salt films.

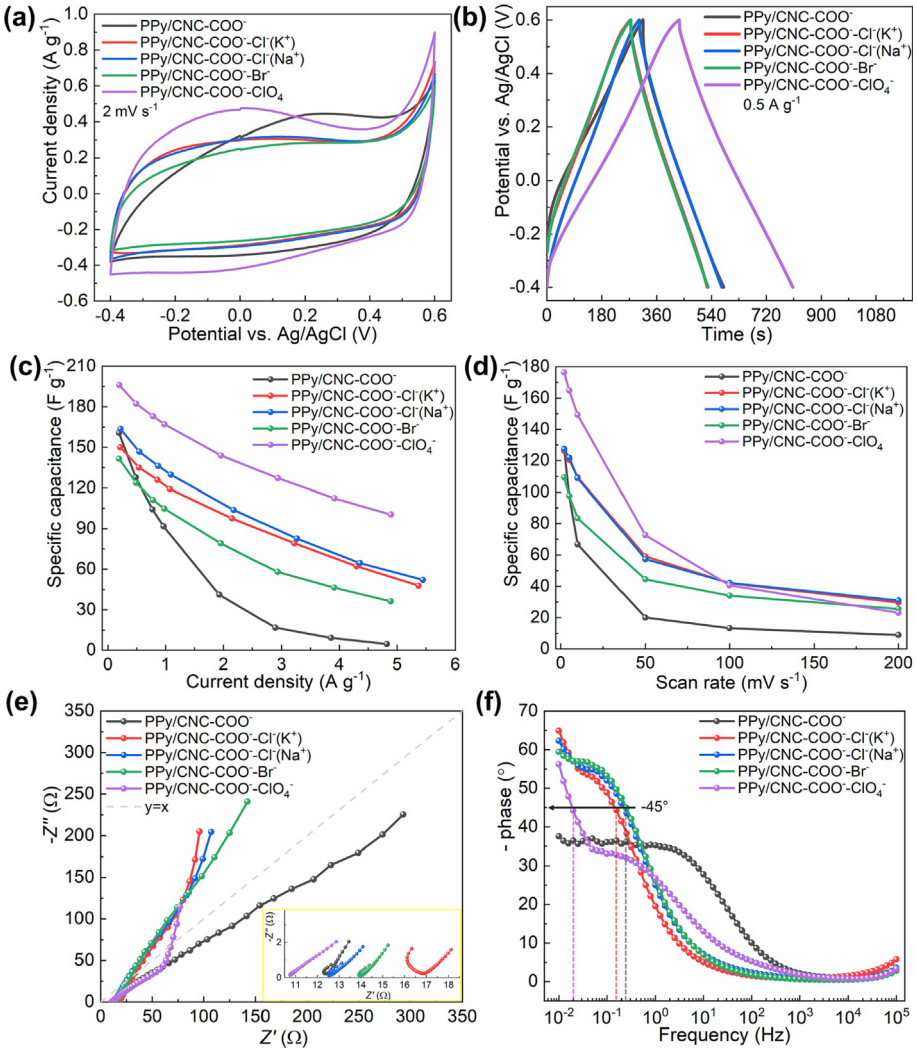

Fig. 4. (a) Cyclic voltammograms of PPy/CNC-COO⁻-salt films at a scan rate of 2 mV s^{-1} in 1 M KCl. (b) Galvanostatic charge/discharge plots of PPy/CNC-COO⁻-salt films at a current density of 0.5 A g^{-1} between −0.4 and 0.6 V vs. Ag/AgCl (3 M KCl) in 1 M KCl. Evolution of specific capacitance with (c) current density and (d) scan rate of PPy/CNC-COO⁻-salt films. (e) Nyquist plot of PPy/CNC-COO⁻-salt films, the insert shows the enlarged image of the high-frequency part. (f) Bode plot of PPy/CNC-COO⁻-salt films.

the arrow shows), resulting in an increased area of the CV plots, implying that more charges were stored during cycling. CV plots of PPy/CNC-COO⁻-Cl⁻(ClO_4^-) films at other scan rates between 2 and 200 mV s^{-1} are combined in Fig. S6. The prolonged charge/discharge time for PPy/CNC-COO⁻-Cl⁻(ClO_4^-) films (Fig. 5d) suggests an increase in capacitance with the addition of $NaClO_4$ into the

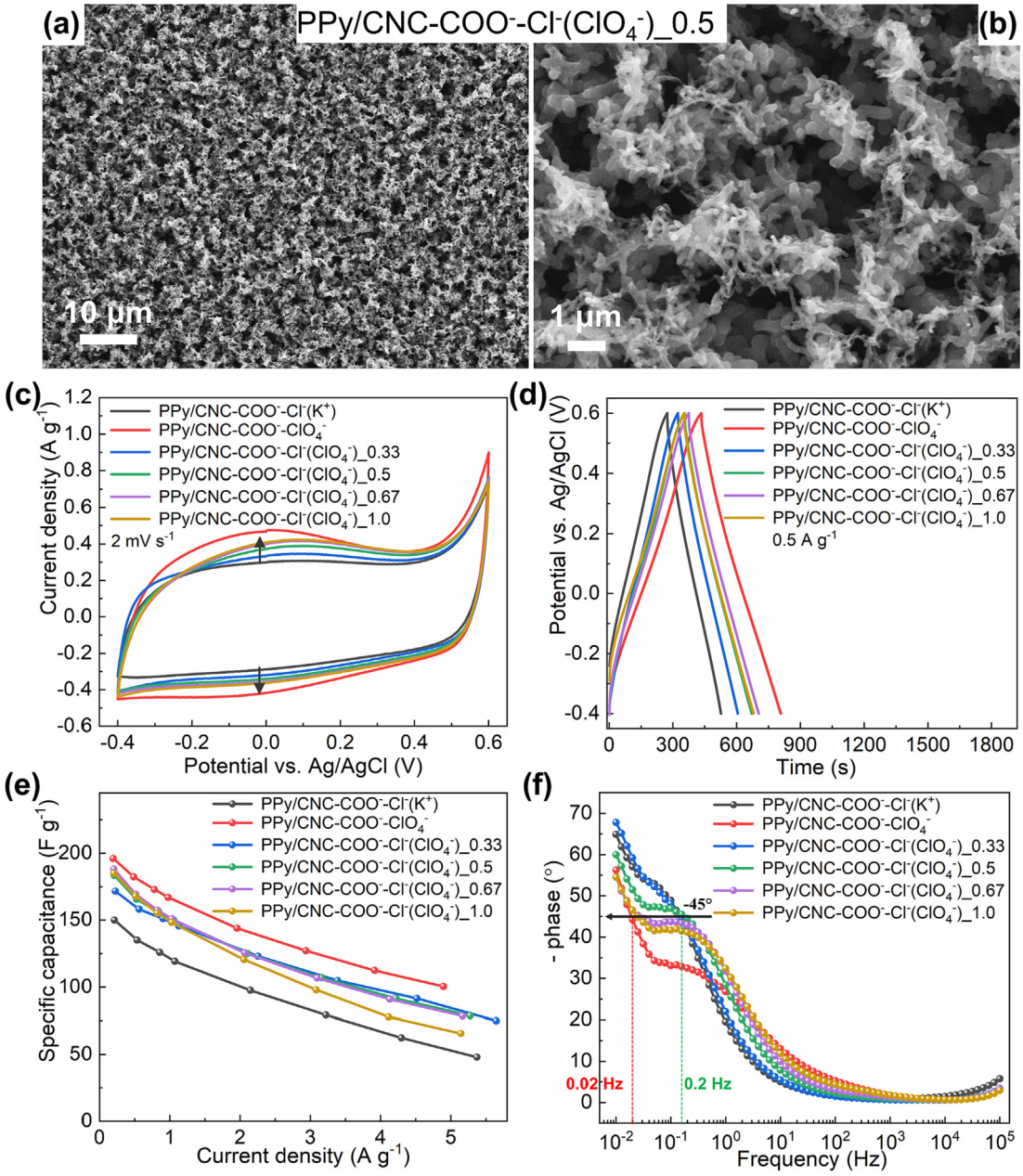

Fig. 5. SEM images of PPy/CNC-COO⁻-Cl⁻(ClO_4^-)_0.5 films at (a) low and (b) high magnification. (c) Cyclic voltammograms of PPy/CNC-COO⁻-Cl⁻(ClO_4^-) films at a scan rate of 2 mV s^{-1} in 1 M KCl. (d) Galvanostatic charge/discharge plots of PPy/CNC-COO⁻-Cl⁻(ClO_4^-) films at a current density of 0.5 A g^{-1} between −0.4 and 0.6 V vs. Ag/AgCl (3 M KCl) in 1 M KCl. (e) Evolution of specific capacitance with the current density and (f) bode plot of PPy/CNC-COO⁻-Cl⁻(ClO_4^-) films.

Py, CNC-COO⁻, and KCl electrolyte. From the evolution plots of the specific capacitance with current density (Fig. 5e), one can see that the PPy/CNC-COO⁻-Cl⁻(ClO_4^-)_0.5 film (6.1 mg cm^{-2}) exhibited a high capacitance of 183.4 F g^{-1} at 0.2 A g^{-1} (1.1 F cm^{-2} at 2 mA cm^{-2}). More importantly, at a high current density of 2.0 A g^{-1} (20 mA cm^{-2}), the PPy/CNC-COO⁻-Cl⁻(ClO_4^-)_0.5 films still retained a specific capacitance of 125.0 F g^{-1} (0.78 F cm^{-2}), increasing almost 204% over PPy/CNC-COO⁻ films (28.2% over PPy/CNC-COO⁻-Cl⁻(K^+) film). These films could finish the charge/discharge process in two min. The improved rate capability of the PPy/CNC-COO⁻-Cl⁻(ClO_4^-)_0.5 films is also clear from its Bode plot, a high knee frequency at a phase angle of −45° occurred at 0.2 Hz, 10 times higher than for the PPy/CNC-COO⁻-ClO_4^- film. The higher phase angle (−60° at 0.01 Hz) of the PPy/CNC-COO⁻-Cl⁻(ClO_4^-)_0.5 films compared to the PPy/CNC-COO⁻-ClO_4^- films implies reduced diffusion and electrical resistance. As a result, by adding $NaClO_4$ and KCl simultaneously into the deposition electrolyte, we deposited the PPy/CNC-COO⁻-Cl⁻(ClO_4^-)_0.5 films with a higher specific capacitance than the PPy/CNC-COO⁻-Cl⁻(K^+) films, combined with a higher rate capability and lower diffusion resistance than the PPy/CNC-COO⁻-ClO_4^- films.

3.3. Electrochemical performance of assembled aqueous supercapacitors

The electrochemical performance of the PPy/CNC-COO⁻-ClO_4^- and PPy/CNC-COO⁻-Cl⁻(ClO_4^-)_0.5 aqueous symmetric SCs is illustrated in Fig. 6. From CV plots (Fig. 6a and b), we could see that the PPy/CNC-COO⁻-Cl⁻(ClO_4^-)_0.5 SC occupied a larger area at high scan rates than the PPy/CNC-COO⁻-ClO_4^- SC, especially at 200 mV s^{-1}. This suggests that more charges are stored in the PPy/CNC-COO⁻-Cl⁻(ClO_4^-)_0.5 SC at high scan rates. The linear

and quasi-symmetric charge/discharge plots (Fig. 6c and d) imply a fast charge/discharge speed of both SCs. From the discharge plot, the PPy/CNC-COO$^-$-ClO_4^- SC exhibited a more pronounced IR drop than the PPy/CNC-COO$^-$-Cl$^-$(ClO_4^-)_0.5 SC. The IR drop for the two SCs is shown in Fig. 6(e), demonstrating a positive relationship with the SCs' equivalent series resistance (R_{ES}) and time constant (τ) following Eqs. (3) and (4). The time constant reflects the responsiveness of the device, i.e., the smaller τ, the faster the responsiveness of the device [32]. τ of the PPy/CNC-COO$^-$-Cl$^-$(ClO_4^-)_0.5 SC is 4.7 s at 2.0 A g^{-1}, close to values for commercial SCs, where τ ranges from 0.5 to 3.6 s. The highest cell capacitance reached was 38.3 F g^{-1} (0.23 F cm^{-2}) and 37.4 F g^{-1} (0.25 F cm^{-2}) at 0.1 A g^{-1} for PPy/CNC-COO$^-$-ClO_4^- and PPy/CNC-COO$^-$-Cl$^-$(ClO_4^-)_0.5 SC, respectively (Fig. 6f).

The cycling stability of the two SCs was tested at 2 A g^{-1} (20 mA cm^{-2}) in 1 M aqueous KCl (Fig. 7a). After 3000 cycles, the PPy/CNC-COO$^-$-ClO_4^- SC retained 77.5% of its initial capacitance, similar to reported results in the literature for PPy SCs [15,20]. The capacitance of the SC increased during the first 500 cycles, ascribed to structural rearrangement of PPy resulting in improved ion transport inside PPy [23,25,47–49]. For the SC with a more porous and interconnected structure (PPy/CNC-COO$^-$-Cl$^-$(ClO_4^-)_0.5 SC), the capacitance retained 113.0% of the original capacitance after 3000 cycles. The full initial capacitance was maintained after 5000 cycles, a value higher than most reported PPy composite electrodes in the literature, as summarized in Table 2 [6–9,15,38,50–53]. The PPy/CNC-COO$^-$-Cl$^-$(ClO_4^-)_0.5 SC showed a similarly improved capacitance as the PPy/CNC-COO$^-$-ClO_4^- SC at the beginning. It seems that the interconnected structure formed by rigid CNC-COO$^-$, KCl, $NaClO_4$, and PPy could resist the structural degradation of PPy better than the discrete structure of the PPy/CNC-COO$^-$-ClO_4^- SC during repeated charge/discharge cycling. From

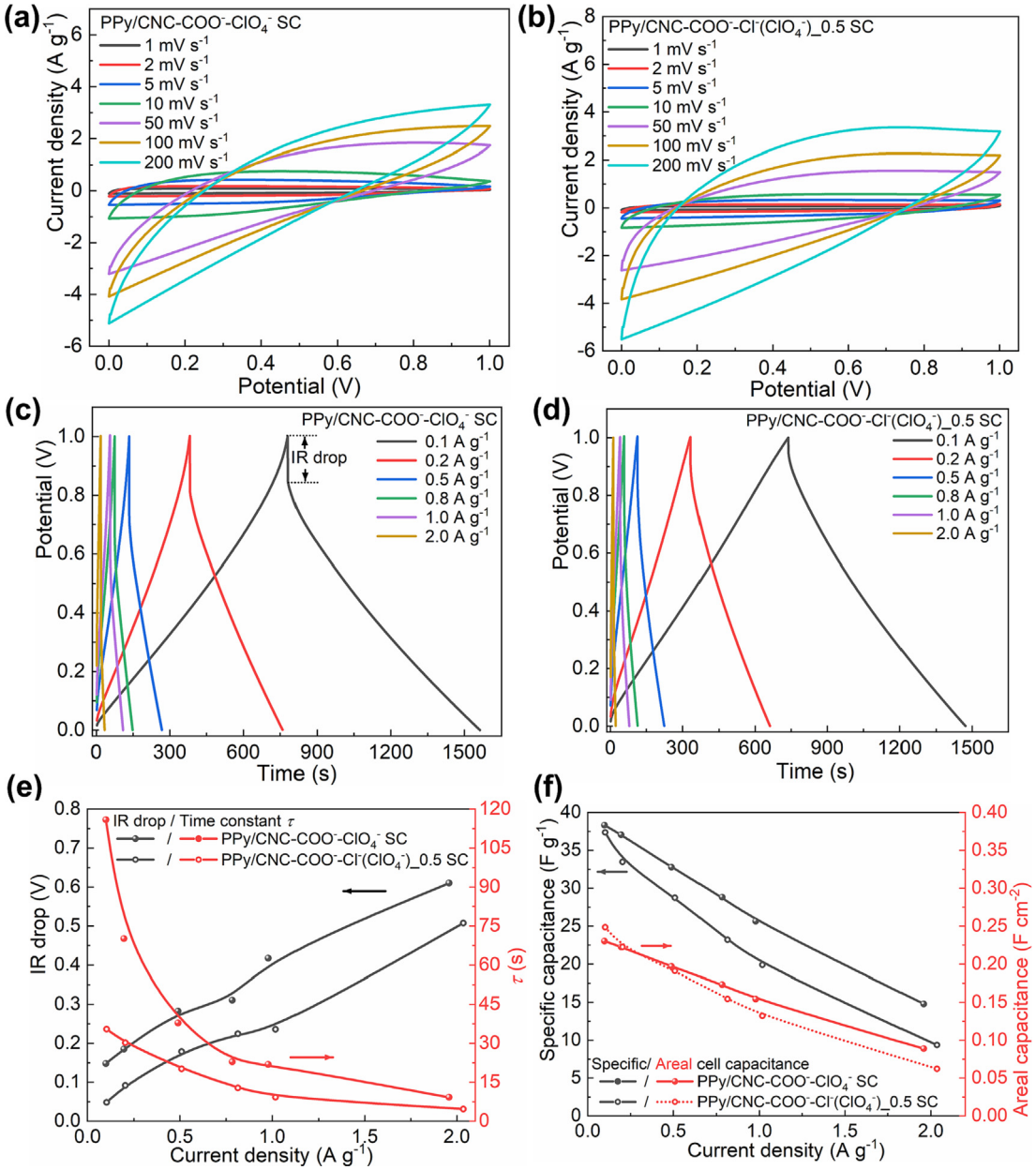

Fig. 6. Electrochemical performance of aqueous symmetric SCs. Cyclic voltammograms of (a) the PPy/CNC-COO$^-$-ClO_4^-, and (b) the PPy/CNC-COO$^-$-Cl$^-$(ClO_4^-)_0.5 SC at different scan rates in 1 M KCl. Galvanostatic charge/discharge plots of (c) the PPy/CNC-COO$^-$-ClO_4^-, and (d) the PPy/CNC-COO$^-$-Cl$^-$(ClO_4^-)_0.5 SC at different current densities between 0 and 1 V in 1 M KCl. (e) Time constant, (f) specific, and areal capacitance of the PPy/CNC-COO$^-$-ClO_4^- and PPy/CNC-COO$^-$-Cl$^-$(ClO_4^-)_0.5 SCs.

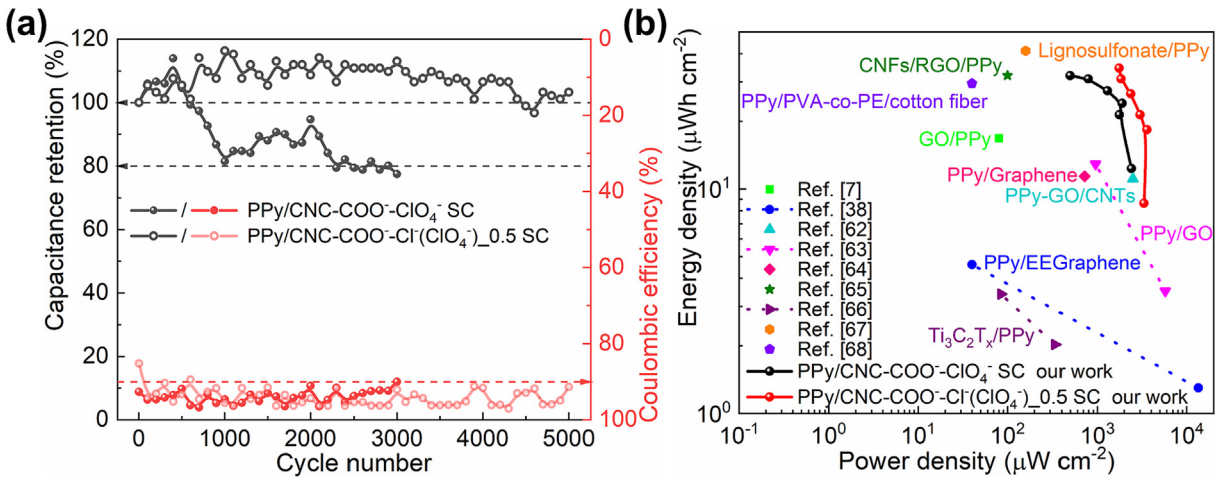

Fig. 7. Cycling stability and Ragone plots of aqueous symmetric SCs. (a) Cycling stability, Coulombic efficiency, and (b) Ragone plot of the PPy/CNC-COO^--ClO_4^- SC and PPy/CNC-COO^--$Cl^-(ClO_4^-)$_0.5.

Table 2
Cycling stability of PPy composite electrode materials reported in the literature.

Samples	Cycling stability	Ref.
MnO_2/PPy composite electrodes	71.2% retention after 500 cycles at 1A g^{-1} in 1 M Na_2SO_4	[53]
EX-GF/PPy-NMS electrodes	91% retention after 1000 cycles at 5 A g^{-1} in 3 M KCl	[15]
PPy/$Ti_3C_2T_x$ SC	85.6% retention after 5000 cycles at 5 A g^{-1} in PVA-H_2SO_4 gel	[9]
Fe_2O_3@PPy//MnO_2 SC	97.1% retention after 3000 cycles at 3 A g^{-1} in 0.5 M Na_2SO_4	[50]
PPy/EEG SC	81.4% retention after 5000 cycles at 6 mA cm^{-2} in 1 M KCl	[38]
PPy/p-TSA SC	88% retention after 6000 cycles at 0.5 A g^{-1} in PVA-H_2SO_4 gel	[6]
3D PPy/GO SC	84.8% retention after 5000 cycles at 10 mA cm^{-2} in 1 M KCl	[7]
PPy/cellulose electrodes	82% retention after 1000 cycles at 0.4 A g^{-1} in 1 M NaCl	[51]
MnO_2@PPy//AC@ACFC SC	90.3% retention after 6000 cycles at 3 A g^{-1} in 1 M Na_2SO_4	[8]
PPy@NCF SC	93% retention after 5000 cycles at 30 mA cm^{-2} in 2 M NaCl	[52]
PPy/CNC-COO^--ClO_4^- SC	77.5% retention after 3000 cycles at 2 A g^{-1} in 1 M KCl	Our work
PPy/CNC-COO^--$Cl^-(ClO_4^-)$_0.5 SC	103.3% retention after 5000 cycles at 2 A g^{-1} in 1 M KCl	

SEM and EDS analysis, we could discern no obvious changes in morphology and composition for either of the SCs before and after the cycling test (Fig. S7).

The energy and power density of two SCs were calculated based on the mass and area of both electrodes. The PPy/CNC-COO^--ClO_4^- device reached the maximum energy power of 489.5 W kg^{-1} at an energy density of 2.1 Wh kg^{-1}, and a superior energy density of 5.3 Wh kg^{-1} at a power density of 24.5 W kg^{-1}. The PPy/CNC-COO^--$Cl^-(ClO_4^-)$_0.5 device could deliver the highest energy density of 5.2 Wh kg^{-1} at a power density of 25.4 W kg^{-1}; this value is almost comparable to the PPy/CNC-COO^--ClO_4^- device, and also higher than some previously reported PPy based SCs, such as the PPy/NFs/PET symmetric SC (3.38 Wh kg^{-1} at 141.4 W kg^{-1}) [54], PPy/nanocellulose SC (3 Wh kg^{-1}) [55], PPy/MWCNT SC (4.5 Wh kg^{-1}) [56], CNT/PPy/Hydroquinone SC (4.7 Wh kg^{-1}) [57], the sulfonated graphene/PPy SC (4.3 Wh kg^{-1} at 108.9 W kg^{-1}) [58], PPy/GO nanocellulose SC (5.1 Wh kg^{-1} at 1500 W kg^{-1}) [59], the PPy SC (4.22 Wh kg^{-1} at 257.91 W kg^{-1}) [60], and PPy hydrogel SC (4.13 Wh kg^{-1} at 270 W kg^{-1}) [61]. The PPy/CNC-COO^--$Cl^-(ClO_4^-)$_0.5 device also had a high area energy density, from 34.5 μWh cm^{-2} at 1752.3 μW cm^{-2} to 8.6 μWh cm^{-2} at 3331.8 μW cm^{-2}, much better than some PPy related reports in the literature, as shown in Fig. 7(b) [7,38,62–68].

4. Conclusions

By adding different commonly used salts into the carboxylated cellulose nanocrystals (CNC-COO^-)-pyrrole solution during electropolymerization, porous and interconnected PPy films were fabricated by simple one-step electrodeposition. Different electrochemical performances of PPy/CNC-COO^--salt film resulted from the inclusion of the different anions (dopants) present in the electrolytes. By adding $NaClO_4$ and KCl simultaneously into the deposition electrolyte, the performance of PPy/CNC-COO^--salt electrode films was significantly improved. PPy/CNC-COO^--$Cl^-(ClO_4^-)$_0.5 films had a high specific capacitance of 183.4 F g^{-1} at 0.2 A g^{-1} (1.1 F cm^{-2} at 2 mA cm^{-2}), an increase of 22% over the PPy/CNC-COO^--$Cl^-(K^+)$ films. Meanwhile, PPy/CNC-COO^--$Cl^-(ClO_4^-)$_0.5 films exhibited a higher rate capability and lower diffusion resistance than PPy/CNC-COO^--ClO_4^- films. After assembling, a PPy/CNC-COO^--$Cl^-(ClO_4^-)$_0.5 SC showed a high energy density of 5.2 Wh kg^{-1} at a power density of 25.4 W kg^{-1} (34.5 μWh cm^{-2} at 1752.3 μW cm^{-2}) based on the whole mass (or area) of two electrodes. The PPy/CNC-COO^--$Cl^-(ClO_4^-)$ _0.5 SC also showed excellent cycling stability, with about 103% capacitance retention after 5000 cycles. Our strategy provides a simple and practical way to design and fabricate PPy-based supercapacitors with high capacitance and ultra-stable cycling ability.

Declaration of competing interest

The authors declare that they have no known competing financial interests or personal relationships that could have appeared to influence the work reported in this paper.

Acknowledgments

This work was supported by the Research Foundation Flanders (grant 3E181170). Z.X. Sun is supported by the China Scholarship Council (CSC, 201806220066). All raw data for this manuscript

can be found at this link: https://doi.org/10.48804/KQBK3R, KU Leuven RDR.

Appendix A. Supplementary data

Supplementary data to this article can be found online at https://doi.org/10.1016/j.jechem.2022.09.024.

References

[1] G.A. Snook, P. Kao, A.S. Best, J. Power Sources 196 (2011) 1–12.
[2] Y. Huang, H. Li, Z. Wang, M. Zhu, Z. Pei, Q. Xue, Y. Huang, C. Zhi, Nano Energy 22 (2016) 422–438.
[3] L. Zhang, W. Du, A. Nautiyal, Z. Liu, X. Zhang, Sci. China Mater. 61 (2018) 303–352.
[4] J. Kim, J. Lee, J. You, M.S. Park, M.S. Al Hossain, Y. Yamauchi, J.H. Kim, Mater. Horizons 3 (2016) 517–535.
[5] Q. Meng, K. Cai, Y. Chen, L. Chen, Nano Energy 36 (2017) 268–285.
[6] M. Zhang, A. Nautiyal, H. Du, J. Li, Z. Liu, X. Zhang, R. Wang, Electrochim. Acta 357 (2020) 136877.
[7] J. Cao, Y. Wang, J. Chen, X. Li, F.C. Walsh, J.H. Ouyang, D. Jia, Y. Zhou, J. Mater. Chem. A 3 (2015) 14445–14457.
[8] W. He, C. Wang, F. Zhuge, X. Deng, X. Xu, T. Zhai, Nano Energy 35 (2017) 242–250.
[9] L. Tong, C. Jiang, K. Cai, P. Wei, J. Power Sources 465 (2020) 228267.
[10] H.N. Wang, M. Zhang, A.M. Zhang, F.C. Shen, X.K. Wang, S.N. Sun, Y.J. Chen, Y.Q. Lan, ACS Appl. Mater. Interfaces 10 (2018) 32265–32270.
[11] J. Li, Z. Zhu, Y. Huang, F. Wang, M.S. Jie, T. Balogun, Mater. Today Energy 26 (2022) 101001.
[12] H. Yang, T. Xiong, Z. Zhu, R. Xiao, X. Yao, Y. Huang, M.S. Balogun, Carbon Energy (2022) 1–13.
[13] S.I. El-Hout, S.Y. Attia, S.G. Mohamed, S.M. Abdelbasir, J. Environ. Manage. 304 (2022) 114222.
[14] R.A. Geioushy, S.Y. Attia, S.G. Mohamed, H. Li, O.A. Fouad, J. Energy Storage 48 (2022) 104034.
[15] Y. Song, J.L. Xu, X.X. Liu, J. Power Sources 249 (2014) 48–58.
[16] Z.H. Chang, D.Y. Feng, Z.H. Huang, X.X. Liu, Chem. Eng. J. 337 (2018) 552–559.
[17] T.F. Otero, M. Alfaro, V. Martinez, M.A. Perez, J.G. Martinez, Adv. Funct. Mater. 23 (2013) 3929–3940.
[18] T.F. Otero, J.G. Martinez, Adv. Funct. Mater. 24 (2014) 1259–1264.
[19] M. Zhu, Y. Huang, Q. Deng, J. Zhou, Z. Pei, Q. Xue, Y. Huang, Z. Wang, H. Li, Q. Huang, C. Zhi, Adv. Energy Mater. 6 (2016) 1600969.
[20] T. Liu, L. Finn, M. Yu, H. Wang, T. Zhai, X. Lu, Y. Tong, Y. Li, Nano Lett. 14 (2014) 2522–2527.
[21] Y. Huang, M. Zhu, W. Meng, Y. Fu, Z. Wang, Y. Huang, Z. Pei, C. Zhi, RSC Adv. 5 (2015) 33981–33989.
[22] C. Yang, J. Shen, C. Wang, H. Fei, H. Bao, G. Wang, J. Mater. Chem. A 2 (2014) 1458–1464.
[23] Y. Song, T.Y. Liu, X.X. Xu, D.Y. Feng, Y. Li, X.X. Liu, Adv. Funct. Mater. 25 (2015) 4626–4632.
[24] S.Y. Liew, D.A. Walsh, W. Thielemans, RSC Adv. 3 (2013) 9158–9162.
[25] Z. Sun, S. Eyley, Y. Guo, R. Salminen, W. Thielemans, J. Energy Chem. 70 (2022) 492–501.
[26] S. Eyley, W. Thielemans, Nanoscale 6 (2014) 7764–7779.
[27] Z. Wang, P. Tammela, M. Strømme, L. Nyholm, Adv. Energy Mater. 7 (2017) 1–22.
[28] Z. Wang, Y.H. Lee, S.W. Kim, J.Y. Seo, S.Y. Lee, L. Nyholm, Adv. Mater. 33 (2021) 2170217.
[29] J. Araki, M. Wada, S. Kuga, T. Okano, Colloids Surfaces A Physicochem. Eng. Asp. 142 (1998) 75–82.
[30] Y. Habibi, H. Chanzy, M.R. Vignon, Cellulose 13 (2006) 679–687.
[31] S. Li, D. Huang, J. Yang, B. Zhang, X. Zhang, G. Yang, M. Wang, Y. Shen, Nano Energy 9 (2014) 309–317.
[32] S. Zhang, N. Pan, Adv. Energy Mater. 5 (2015) 1–19.
[33] S.Y. Attia, S.G. Mohamed, Electrochim. Acta 407 (2022) 139918.
[34] S.Y. Attia, S.G. Mohamed, Y.F. Barakat, H.H. Hassan, W. Al Zoubi, Rev. Inorg. Chem. 42 (2022) 53–88.
[35] T. Patois, B. Lakard, S. Monney, X. Roizard, P. Fievet, Synth. Met. 161 (2011) 2498–2505.
[36] S.Y. Liew, W. Thielemans, D.A. Walsh, J. Phys. Chem. C 114 (2010) 17926–17933.
[37] C. Peng, J. Jin, G.Z. Chen, Electrochim. Acta 53 (2007) 525–537.
[38] S. Ji, J. Yang, J. Cao, X. Zhao, M.A. Mohammed, P. He, R.A.W. Dryfe, I.A. Kinloch, ACS Appl. Mater. Interfaces 12 (2020) 13386–13399.
[39] Q. Wang, Y. Ma, X. Liang, D. Zhang, M. Miao, J. Mater. Chem. A 6 (2018) 10361–10369.
[40] S. Zhou, P. Huang, T. Xiong, F. Yang, H. Yang, Y. Huang, D. Li, J. Deng, M.S. Balogun, Small 17 (2021) 1–13.
[41] J. Tabačiarová, M. Mičušík, P. Fedorko, M. Omastová, Polym. Degrad. Stab. 120 (2015) 392–401.
[42] M.A. Chougule, S.G. Pawar, P.R. Godse, R.N. Mulik, S. Sen, V.B. Patil, Soft Nanosci. Lett. 01 (2011) 6–10.
[43] S. Sarkar, R. Akshaya, S. Ghosh, Electrochim. Acta 332 (2020) 135368.
[44] L. Yuan, X.H. Lu, X. Xiao, T. Zhai, J. Dai, F. Zhang, B. Hu, X. Wang, L. Gong, J. Chen, C. Hu, Y. Tong, J. Zhou, Z.L. Wang, ACS Nano 6 (2012) 656–661.
[45] K. Mahankali, N.K. Thangavel, Y. Ding, S.K. Putatunda, L.M.R. Arava, Electrochim. Acta 326 (2019) 134989.
[46] K. Krishnamoorthy, P. Pazhamalai, S. Sahoo, S.J. Kim, J. Mater. Chem. A 5 (2017) 5726–5736.
[47] R. Ansari, E-Journal Chem. 3 (2006) 186–201.
[48] P. Pfluger, M. Krounbi, G.B. Street, G. Weiser, J. Chem. Phys. 78 (1983) 3212–3218.
[49] R.K. Singh, A. Kumar, K. Agarwal, M. Kumar, H.K. Singh, P. Srivastava, R. Singh, J. Polym. Sci. Part B Polym. Phys. 50 (2012) 347–360.
[50] P.Y. Tang, L.J. Han, A. Genç, Y.M. He, X. Zhang, L. Zhang, J.R. Galán-Mascarós, J.R. Morante, J. Arbiol, Nano Energy 22 (2016) 189–201.
[51] S. Liu, K. He, X. Wu, X. Luo, B. Li, RSC Adv. 5 (2015) 87266–87276.
[52] Z. Wang, D.O. Carlsson, P. Tammela, K. Hua, P. Zhang, L. Nyholm, M. Strømme, ACS Nano 9 (2015) 7563–7571.
[53] Y. Song, M. Shang, J. Li, Y. Su, Chem. Eng. J. 405 (2021) 127059.
[54] Q. Liu, B. Wang, J. Chen, F. Li, K. Liu, Y. Wang, M. Li, Z. Lu, W. Wang, D. Wang, F. Li, K. Liu, Y. Wang, M. Li, Z. Lu, W. Wang, D. Wang, Compos. Part A Appl. Sci. Manuf. 101 (2017) 30–40.
[55] Z. Wang, P. Tammela, P. Zhang, M. Strømme, L. Nyholm, J. Mater. Chem. A 2 (2014) 7711–7716.
[56] Y. Su, I. Zhitomirsky, Appl. Energy 153 (2015) 48–55.
[57] R. Xu, F. Guo, X. Cui, L. Zhang, K. Wang, J. Wei, J. Mater. Chem. A 3 (2015) 22353–22360.
[58] X. Zuo, Y. Zhang, L. Si, B. Zhou, B. Zhao, L. Zhu, X. Jiang, J. Alloys Compd. 688 (2016) 140–148.
[59] Z. Wang, P. Tammela, M. Strømme, L. Nyholm, Nanoscale 7 (2015) 3418–3423.
[60] W.K. Chee, H.N. Lim, I. Harrison, K.F. Chong, Z. Zainal, C.H. Ng, N.M. Huang, Electrochim. Acta 157 (2015) 88–94.
[61] J. Bo, X. Luo, H. Huang, L. Li, W. Lai, X. Yu, J. Power Sources 407 (2018) 105–111.
[62] H. Zhou, G. Han, Electrochim. Acta 192 (2016) 448–455.
[63] H. Zhou, G. Han, Y. Xiao, Y. Chang, H.J. Zhai, J. Power Sources 263 (2014) 259–267.
[64] K. Qi, R. Hou, S. Zaman, B.Y. Xia, H. Duan, J. Mater. Chem. A 6 (2018) 3913–3918.
[65] Y. Zhang, Z. Shang, M. Shen, S.P. Chowdhury, A. Ignaszak, S. Sun, Y. Ni, A.C.S. Sustain, Chem. Eng. 7 (2019) 11175–11185.
[66] C. Zhang, S. Xu, D. Cai, J. Cao, L. Wang, W. Han, Electrochim. Acta 330 (2020) 135277.
[67] Z. Peng, C. Wang, Z. Zhang, W. Zhong, Adv. Mater. Interfaces 6 (2019) 1–12.
[68] D. Sun, Q. Liu, C. Yi, J. Chen, D. Wang, Y. Wang, X. Liu, M. Li, K. Liu, P. Zhou, G. Sun, Electrochim. Acta 354 (2020) 136746.